





Symmetry-protected topological exceptional chains in non-Hermitian crystals

Ruo-Yang Zhang ^{1,3}✉, Xiaohan Cui ^{1,3}, Wen-Jie Chen ², Zhao-Qing Zhang¹ & C. T. Chan ¹✉

In non-Hermitian systems, defective band degeneracies called exceptional points can form exceptional lines (ELs) in 3D momentum space in the absence of any symmetries. However, whether the presence of symmetries can affect the EL configurations had rarely been discussed. Here we show that a natural orientation can be assigned to every EL according to the eigenenergy braiding around it, and we establish the source-free principle of ELs stating that the number of ELs ingoing and outgoing from the junction must be conserved. Based on this principle, we discover that three crystalline-symmetry-based mechanisms can stabilize the junction of ELs, resulting in the formation of various types of exceptional chains (ECs). We further demonstrate that ECs can be observed in prototypical non-Hermitian photonic crystals. Our results combine the effect of non-Hermitian spatiotemporal symmetry and topology to pave the way for understanding and manipulating the morphology of ELs in non-Hermitian crystalline systems.

¹Department of Physics, The Hong Kong University of Science and Technology, Hong Kong, China. ²School of Physics & State Key Laboratory of Optoelectronic Materials and Technologies, Sun Yat-sen University, Guangzhou 510275, China. ³These authors contributed equally: Ruo-Yang Zhang and Xiaohan Cui. ✉email: ruoyangzhang@ust.hk; phchan@ust.hk

In topological physics, an important direction is to study topologically protected degeneracies with different dimensions in the band structure^{1–4}. In addition to being manifestations of hypothetical quasi-particles originally proposed in fundamental physics, these degeneracies also induce novel transport effects that have broad application potential. As impressive progress has been made in understanding Hermitian gapless topology in the past decades, non-Hermitian degeneracies are increasingly attracting interest from diverse disciplines of physics, especially photonics^{5–9} and condensed matter physics^{10–16}. In marked contrast to the Hermitian band crossings, non-Hermitian bands can be degenerate at exceptional points (EPs) where both the eigenenergies and eigenvectors of different bands coalesce^{16–19}. Owing to their fascinating physical properties, EPs have given rise to versatile functionalities, such as ultra-sensitive sensing^{20–23}, chiral non-adiabatic transport^{24–27}, and unidirectional lasing^{28–30}. From the perspective of topology, EPs are essentially the topological obstructions to sorting the complex-valued energy bands. When traveling around EPs, the eigenenergies braid about each other, swapping order, and may eventually fail to return to their initial states after going around a full loop. As uncovered by recent studies, this eigenenergy braiding along 1D loops faithfully characterizes the topological classification of the non-Hermitian gapless phases associated with EPs^{31–38}.

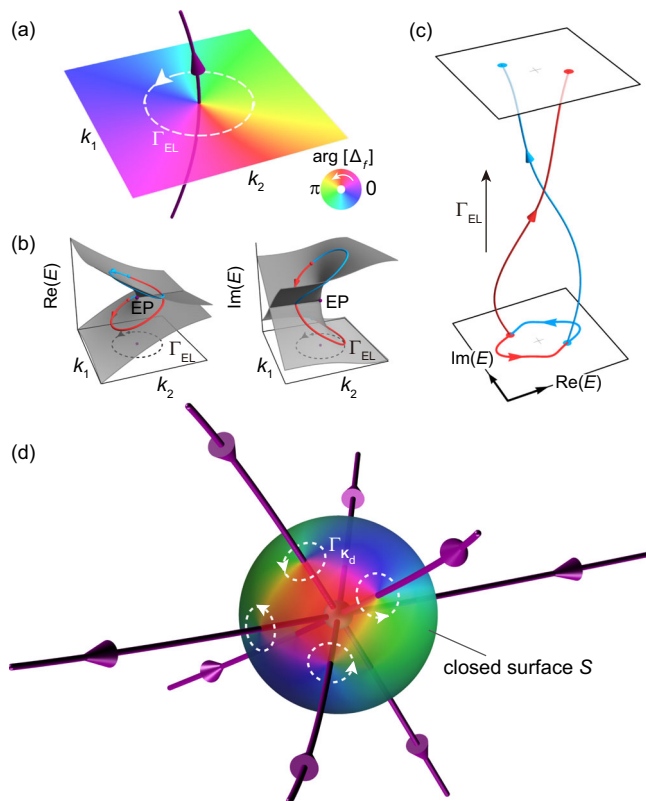


Fig. 1 Orientation of exceptional lines (ELs) and source-free principle. **a** An order-2 EL manifests as the phase singularity of the discriminant $\Delta_f(\mathbf{k})$, where the sign of phase vortex assigns a positive orientation (arrow on the EL) to the EL in compliance with the right-hand rule of the loop Γ_{EL} (white dashed). **b** Real and imaginary parts of two intersecting bands on the transverse plane in **(a)**, and the red and light-blue trajectories denote the two modes along the path Γ_{EL} . **c** Braiding and mode switching of two eigenenergies along the loop Γ_{EL} in **(a)**. **d** Schematic of the generalized doubling theorem for exceptional points. Several directed ELs meet at a junction that is enclosed by a surface S . Colormap on the surface: $\arg[\Delta_f(\mathbf{k})]$.

In three-dimensional (3D) non-Hermitian systems, the order-2 EPs can generally trace out robust curves, known as exceptional lines (ELs)^{39–42}, in the momentum space even in the absence of any symmetries. Specifically, it has been shown that ELs can be knotted or linked together in nontrivial ways^{43–49}, analogous to Hermitian nodal knots and nodal links^{50–53}. However, as the counterpart of Hermitian nodal chains^{54–59}, exceptional chains (ECs), formed by several connected ELs, have a fundamental difference from other EL configurations, i.e., the existence and stability of ECs demand symmetry protection. Although the connection or intersection of ELs was accidentally observed in a few very recent works^{60–62}, the underlying mechanisms of symmetry and topology had rarely been discussed. As a result, the mystery of EC formation remains unraveled until now.

In this work, we reveal that the complex eigenenergy braiding around an EL can assign a positive orientation to the EL, inspired by the recent breakthrough of the Hermitian nodal chain and link theory^{63–69}. Via generalizing the Fermion doubling theorem of EPs³⁴ to arbitrarily oriented and closed surfaces, we prove that the directed ELs are always source-free in the 3D momentum space. As an immediate application, the source-free principle together with certain non-Hermitian spatiotemporal symmetries can enforce several directed ELs to be robustly chained with each other in order to keep the balance between inward and outward ELs at the chain point. We uncover that by incorporating the Hermitian-adjoint into account, the non-Hermitian crystalline systems are generically described by double-antisymmetry (DAS) space groups^{70–72}, and we propose three DAS point-group symmetry-based mechanisms that can stabilize different types of ECs, termed orthogonal ECs, planar ECs, and mirror-symmetric ECs, respectively, which have distinct local morphologies and topological features. In particular, we show that in forming these ECs, both eigenvalue-based and eigenvector-based topologies play pivotal roles, explaining the richer diversity of ECs than Hermitian nodal chains. Starting with a Hermitian nodal ring, we also study the evolution roadmap toward various types of ECs by introducing thresholdless non-Hermitian perturbations. In addition, we design non-Hermitian photonic crystals (PCs) to illustrate our ideas of symmetry-protected ECs. Through numerical simulations, three typical ECs i.e. a pair of linked orthogonal EC networks protected by three mirror-adjoint symmetries, a planar EC with four non-defected chain points, and a double-earring EC protected by mirror-adjoint and $C_2\mathcal{T}$ symmetries, are observed in the PCs, hence confirming the applicability of our theory for general full-wave systems.

Results

Orientations of exceptional lines. Unlike nodal lines in Hermitian systems whose existence requires symmetry protection^{3,4}, a line of order-2 EPs in 3D momentum space can be topologically stable in the absence of any symmetries¹³, where the two crossing energy bands, E_i , E_{i+1} , braid about each other and swap their order along a loop Γ_{EL} encircling the EL (see Fig. 1a–c). The eigenenergy braiding around an EL can be characterized by the half-quantized interband energy vorticity^{10,13} $\nu_{i,i+1}(\Gamma_{EL}) = \frac{1}{2\pi} \oint_{\Gamma_{EL}} d\mathbf{k} \cdot \nabla_{\mathbf{k}} \arg[E_i(\mathbf{k}) - E_{i+1}(\mathbf{k})] = \pm \frac{1}{2}$. The sign of the energy vorticity of the two intertwining bands endows such an elementary EL with a positive orientation, as indicated by the arrows on the ELs in Fig. 1:

$$\mathbf{t}_{EL} = \text{sign}[\nu_{i,i+1}(\Gamma_{EL})]\mathbf{t}_{\Gamma}, \quad (1)$$

where \mathbf{t}_{Γ} is a tangent vector of the EL in compliance with the right-hand rule of the directed loop Γ_{EL} .

For a generic multi-band Bloch Hamiltonian $\mathcal{H}(\mathbf{k})$, a \mathbb{Z} topological invariant, dubbed as discriminant number (DN)³⁴,

was recently introduced to demarcate non-Hermitian topological phases on a 1D closed sub-manifold (a closed path Γ), which is defined as the sum of all interband vorticities $\nu_{ij}(\Gamma)$ along the path, and is equivalent to the phase winding number of the discriminant $\Delta_f(\mathbf{k}) = \prod_{i<j} [E_i(\mathbf{k}) - E_j(\mathbf{k})]^2$ of the Hamiltonian's characteristic polynomial $f(E, \mathbf{k}) = \det[E - \mathcal{H}(\mathbf{k})]$ ^{31,34},

$$\mathcal{D}(\Gamma) = \sum_{i \neq j} \nu_{ij}(\Gamma) = 2 \sum_{i < j} \nu_{ij}(\Gamma) = \frac{-i}{2\pi} \oint_{\Gamma} d\mathbf{k} \cdot \nabla_{\mathbf{k}} \Delta_f(\mathbf{k}). \quad (2)$$

Once $\mathcal{D}(\Gamma) \neq 0$, there exist lines of degenerate points $\{\mathbf{k}_d | \Delta_f(\mathbf{k}_d) = 0\}$ encircled by the loop Γ , prohibiting Γ from shrinking to disappear without closing the gap along the loop.

If the loop Γ only encloses a single EL, the DN is solely contributed by the energy vorticity of the two bands E_i, E_{i+1} forming the EL: $\mathcal{D}(\Gamma) = 2\nu_{i,i+1}(\Gamma) = \pm 1$, then the positive tangent vector of the EL is alternatively expressed as $\mathbf{t}_{\text{EL}} = \mathcal{D}(\Gamma)\mathbf{t}_{\Gamma}$. And for an arbitrary loop Γ in the 3D space, the DN carried by Γ , $\mathcal{D}(\Gamma) \in \mathbb{Z}$, characterizes the net number of the directed ELs, as counted according to their positive directions, enclosed by the loop.

Recent studies unveiled that the braiding of eigenenergies along 1D loops (e.g., Fig. 1c) can faithfully determine the 1D non-Hermitian topology for a generic N -band system with separable bands, and the complete classification of such topological phases is given by the braid group of N strands, B_N , generated by the braid generators b_i ($i \in \{1, 2, \dots, N-1\}$) denoting the braiding between i^{th} and $(i+1)^{\text{th}}$ eigenenergies³¹⁻³³. For an arbitrary 1D loop Γ , the braid element, $b(\Gamma) = b_{i_1}^{n_1} b_{i_2}^{n_2} b_{i_3}^{n_3} \dots \in B_N$, and the DN, $\mathcal{D}(\Gamma) \in \mathbb{Z}$, carried by the loop satisfy the relation (see proof in Supplementary Note 1)

$$\mathcal{D}(\Gamma) = n_1 + n_2 + n_3 + \dots \quad (3)$$

Namely, the DN is equal to the sum of the exponents on the braid generators (also known as the algebraic length of the braid $b(\Gamma)$), representing the net number of times the mode braiding takes place. On the other hand, the total biorthogonal Berry phase of all bands along Γ , known as the global Berry phase $\Theta(\Gamma)$, also assigns a \mathbb{Z}_2 topological invariant to the loop^{33,73}. Whenever the sequences of the initial and final eigenstates, Ψ_0 and Ψ_f , after a cycle along Γ are different up to a permutation $\hat{p}(\Gamma)$, $\Psi_f = \hat{p}(\Gamma)\Psi_0$, the global Berry phase is determined by the parity of the permutation³³, $\det[\hat{p}(\Gamma)] = \pm 1$, and therefore also by the parity of the DN (see proof in Supplementary Note 1):

$$\begin{aligned} \exp[i\Theta(\Gamma)] &= \exp\left[\oint_{\Gamma} d\mathbf{k} \cdot \text{Tr}(\Psi^{-1}\nabla_{\mathbf{k}}\Psi)\right] \\ &= \det[\hat{p}(\Gamma)] = (-1)^{\mathcal{D}(\Gamma)}, \end{aligned} \quad (4)$$

where $\Psi = (|\psi_1^R(\mathbf{k})\rangle, |\psi_2^R(\mathbf{k})\rangle, \dots, |\psi_N^R(\mathbf{k})\rangle)$ and $\Psi^{-1} = (|\psi_1^L(\mathbf{k})\rangle, \dots, |\psi_N^L(\mathbf{k})\rangle)^{\dagger}$ denote the matrices composed of right and left eigenstates at \mathbf{k} , respectively. Thus, the \mathbb{Z}_2 global Berry phase actually describes whether there are even or odd numbers of ELs passing through the loop.

Source-free principle of ELs. Let us consider an orientable closed surface, S , in the 3D Brillouin zone (BZ). We are interested in the net number of ELs penetrating S , as shown by the schematic in Fig. 1d. Because the discriminant $\Delta_f(\mathbf{k})$ is a continuous single-valued function in the whole BZ, mathematically, it serves as a global section on a trivial complex line bundle $\pi : L \cong S \times \mathbb{C} \rightarrow S$ possessing a zero Chern number $\text{Ch}(L) = 0$. Therefore, we infer from the Poincaré–Hopf theorem for complex line bundles^{74,75} that the total DN carried by all isolated degenerate points $\{\mathbf{k}_d\}$ on

the surface must vanish (see Supplementary Note 2),

$$\sum_{\mathbf{k}_d \in S} \mathcal{D}(\Gamma_{\mathbf{k}_d}) = \text{Ch}(L) = 0, \quad (5)$$

where $\Gamma_{\mathbf{k}_d}$ stands for a small directed loop encircling the singularity \mathbf{k}_d whose direction for the integral of DN is consistent with the outward normal of the surface.

If all the degenerate points on S are elementary EPs with $\mathcal{D}(\Gamma_{\mathbf{k}_d}) = \pm 1$, Eq. (5) generalizes the Fermion doubling theorem for EPs³⁴ to arbitrary closed oriented surfaces, i.e., EPs always appear in pairs with opposite DN on a closed oriented surface. The doubling theorem indicates that the ELs are source-free and have to form closed loops in the 3D BZ, which serves as a conservation rule regulating the morphology and evolution of ELs in the 3D space. In particular, if several oriented ELs meet at a junction under some constraints, the doubling theorem on a sufficiently small sphere enclosing the junction informs us that the numbers of inflow and outflow ELs must be equal (Fig. 1d), even though the ELs are formed by different pairs of bands in multi-band systems (see examples in Supplementary Note 9). Next, we will show that the junctions of ELs with various local morphologies can be guaranteed by certain spatiotemporal symmetries.

Symmetry-protected exceptional chains. In previous works on non-Hermitian crystals, the magnetic space groups, including the time reversal operator \mathcal{T} , are usually adopted to characterize the crystalline symmetries and band degeneracies^{76,77}. However, it was revealed recently that Hermitian-adjoint “ \dagger ” could appear as a new dimension that leads to intriguing physical effects and enriches the classification of non-Hermitian topological phases^{12,78}. Here, we uncover that akin to the time-reversal, the Hermitian-adjoint transformation could be regarded as an antisymmetry⁷¹ with respect to the ordinary space groups. Hence by involving both Hermitian-adjoint and time reversal as two antisymmetries, the non-Hermitian crystals can be universally described by DAS space groups⁷⁰⁻⁷² (see Methods for details). In what follows, we introduce three mechanisms to stabilize ECs by DAS point-group symmetries.

Orthogonal ECs protected by Mirror-adjoint ($M\text{-}\dagger$) or $C_2\mathcal{T}$ symmetries. In Hermitian systems, as a prerequisite for chaining different nodal lines together, the line nodes should be confined by symmetries (usually mirror symmetry) in the high-symmetry planes^{63,64,66}. This inspires us that seeking suitable symmetries to fix ELs into planes would be the first step toward an EC. It is known that in a pseudo-Hermitian^{79,80} or parity time-reversal (\mathcal{PT}) symmetric⁸¹ system, the parameter space can be divided into exact and broken phases wherein the eigenenergies are purely real and in complex conjugate pairs, respectively. And EPs always occur at the boundaries between the two phases. Borrowing this mechanism to a 2D subspace, we find that two DAS point-group symmetries, i.e., mirror-adjoint symmetry (denoted $M\text{-}\dagger$) and combined twofold rotation time-reversal symmetry ($C_2\mathcal{T}$), fit the bill.

The $M\text{-}\dagger$ symmetry is a non-Hermitian generalization of mirror symmetry, which is defined as the combination of mirror reflection and Hermitian-adjoint. For the Bloch Hamiltonian $\mathcal{H}(\mathbf{k})$ in the momentum space, it can be expressed as

$$\hat{M}\mathcal{H}(\hat{m}\mathbf{k})\hat{M}^{-1} = \mathcal{H}(\mathbf{k}), \quad (6)$$

where \hat{m} represents the mirror reflection on spatial coordinates and vectors, and \hat{M} is a Hermitian unitary reflection operator on Bloch states. $M\text{-}\dagger$ is an intrinsic non-Hermitian spatial symmetry distinct from the mirror symmetry in non-Hermitian systems,

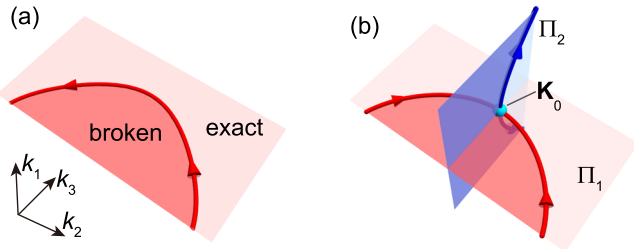


Fig. 2 Orthogonal exceptional chain. **a** Exceptional line (EL) confined in a symmetry-invariant plane by $M-\dagger$ or $C_2\mathcal{T}$ symmetry, separating the exact (light red) and broken (red) phases. **b** Orthogonal exceptional chain protected by two symmetries belonging to $M-\dagger$ or $C_2\mathcal{T}$, where ELs, confined in two perpendicular planes Π_1 and Π_2 connect at the chain point \mathbf{K}_0 . In each plane, the lighter (darker) region denotes the exact (broken) phase.

while they reduce to an identical one in Hermitian cases. On a M -invariant plane $\Pi_M = \{\mathbf{k}_m \in \text{BZ} | \hat{m}\mathbf{k}_m = \mathbf{k}_m\}$, Eq. (6) implies that $\mathcal{H}(\mathbf{k}_m)$ is pseudo-Hermitian. Therefore, as depicted in Fig. 2a, all eigenstates on that plane are classified as being either exact or broken, and the transition boundary of the two phases forms an EL lying in Π_M (see Supplementary Note 4).

Similarly, the bosonic $C_2\mathcal{T}$ symmetry of a Bloch Hamiltonian requires

$$\hat{C}_2 \hat{T} \mathcal{H}(-\hat{c}_2 \mathbf{k})^* (\hat{C}_2 \hat{T})^{-1} = \mathcal{H}(\mathbf{k}), \quad (7)$$

where \hat{c}_2 denotes the corresponding twofold rotation on coordinates and vectors, $\hat{C}_2 \hat{T}$ is the unitary part of the symmetry operator satisfying $(\hat{C}_2 \hat{T})(\hat{C}_2 \hat{T})^* = 1$ as the consequence of $(C_2\mathcal{T})^2 = 1$. On a $C_2\mathcal{T}$ -invariant plane $\Pi_{C_2\mathcal{T}} = \{\mathbf{k}_c \in \text{BZ} | \mathbf{k}_c = -\hat{c}_2 \mathbf{k}_c\}$, the Hamiltonian $\mathcal{H}(\mathbf{k}_c)$ can be considered to be 2D \mathcal{PT} -symmetric, and hence ELs can also be confined in this plane, separating $C_2\mathcal{T}$ exact and broken phases.

In Fig. 2b, we consider a system with two such symmetries $R_1, R_2 \in \{M-\dagger, C_2\mathcal{T}\}$, whose invariant planes Π_1 (red), Π_2 (blue) are perpendicular. Imagining a single EL (red) is fixed by R_1 in the plane Π_1 and cuts through Π_2 at the midpoint \mathbf{K}_0 , R_2 symmetry guarantees this oriented EL to be symmetric about Π_2 . In particular, its orientation must be reversed at \mathbf{K}_0 , say, the two red half-ELs at different sides of Π_2 are both directed toward \mathbf{K}_0 (Fig. 2b), since the DN obeys the relation $\mathcal{D}(\Gamma) = -\mathcal{D}(\hat{R}_2\Gamma)$ (see Supplementary Note 3 for a general discussion of the constraints on EL orientations imposed by different types of DAS point group symmetries). By the source-free requirement of ELs at \mathbf{K}_0 , there should exist at least another EL (blue) on Π_2 with two outflow half-lines connecting the red EL at \mathbf{K}_0 , thereby forming an orthogonal exceptional chain. Accordingly, regions of the exact (broken) phase on the two planes are consistently joined along their intersection. Thus, we have demonstrated that any pair of symmetries belonging to $\{M-\dagger, C_2\mathcal{T}\}$ can protect the existence of orthogonal ECs.

However, if either of the two symmetries is $M-\dagger$, the formation of an orthogonal EC requires the bands to satisfy additional conditions. To see this, we inspect the relation, imposed by the $M-\dagger$ symmetry, to a pair of right and left eigenstates, $|\psi^R(\mathbf{k}_m)\rangle, |\psi^L(\mathbf{k}_m)\rangle$ in the exact phase on a mirror plane Π_M :

$$\hat{M} |\psi^R(\mathbf{k}_m)\rangle = \rho(\mathbf{k}_m) |\psi^L(\mathbf{k}_m)\rangle, \quad (8)$$

where $\rho(\mathbf{k}_m)$ is a nonzero coefficient. Therefore, the expectations of the mirror operator in any pair of right and left eigenvectors always take the same nonzero real value. Then, the sign of mirror expectation invests each pair of eigenstates $|\psi^{R/L}(\mathbf{k}_m)\rangle$ in the

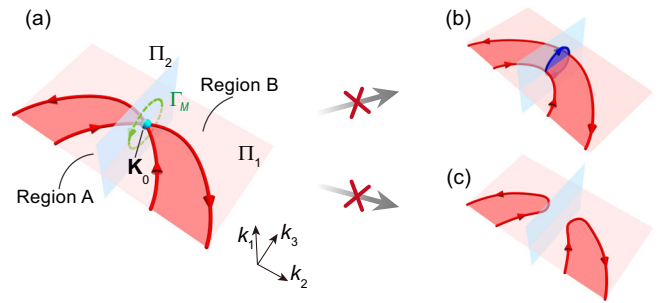


Fig. 3 Planar exceptional chain. **a** Schematic of a planar exceptional chain protected by two mirror-adjoint symmetries ($M_{1,2}-\dagger$). \mathbf{K}_0 is the non-defective chain point confined on the intersection of two mirror planes Π_1 and Π_2 . A and B are two regions of exact phase in Π_1 with opposite $M_1-\dagger$ parities $\tilde{p}_A^+ \tilde{p}_B^+ = -1$. **b, c** Two plausible evolutions compatible with the source-free principle of exceptional lines, which are, however, forbidden by **(b)** the same $M_2-\dagger$ -parity of two bands and by **(c)** the quantized Berry phase along Γ_M , respectively. In each plane, the lighter (darker) region denotes the exact (broken) phase.

exact phase with a certain $M-\dagger$ -parity,

$$\tilde{p}(\mathbf{k}_m) = \text{sign}[\langle \psi^{R/L}(\mathbf{k}_m) | \hat{M} | \psi^{R/L}(\mathbf{k}_m) \rangle] = \pm 1, \quad (9)$$

which generalizes the concept of mirror-parity for the eigenstates in mirror-symmetric systems. Intriguingly, the following theorem can be proved (see Supplementary Note 4).

Theorem 1. A $M-\dagger$ -symmetry-protected order-2 exceptional line on Π_M can only be formed by two bands with opposite $M-\dagger$ -parities in the nearby exact phase.

Consequently, we know from the theorem that an orthogonal EC in Fig. 2b protected either by two $M-\dagger$ symmetries or by $(M-\dagger, C_2\mathcal{T})$ symmetries cannot be formed, unless the $M-\dagger$ -parities of the two crossing bands take opposite signs in the exact phases on the corresponding mirror planes.

Planar ECs protected by two $M-\dagger$ symmetries. In the presence of two orthogonal mirror-adjoint symmetries, denoted $M_1-\dagger$ and $M_2-\dagger$, they can locally stabilize another type of EC, termed planar EC, as shown in Fig. 3a, with two crossing ELs confined in the same mirror plane Π_1 and the chain point is fixed along the intersection of the two mirror planes (the little group along the intersection line is isomorphic to the DAS point group $m^\dagger m^\dagger 2$ [the symbol is the generalization of Hermann-Mauguin (HM) notation for point groups⁷², cf. Methods and Supplementary Note 6]), where the two ELs are formed by the coalescence of two bands whose $M-\dagger$ parities are opposite in the nearby exact phase in Π_1 but are identical in Π_2 .

At first glance, the source-free principle of ELs does not forbid the two possible evolutions shown in Fig. 3b, c. However, the contrapositive of the above theorem indicates that any degeneracy between two bands with the same $M_2-\dagger$ -parity in the exact phase should be non-defective on Π_2 , hence the crossing point \mathbf{K}_0 of the two $M_2-\dagger$ -partner ELs on Π_1 is a non-defective diabolic point banned from expanding to an EP ring in Π_2 (i.e., the case of Fig. 3b). This effect also distinguishes the systems with two $M-\dagger$ symmetries and those with $M_1-\dagger$ and $C_2\mathcal{T}$ symmetries. In the latter case, the $C_2\mathcal{T}$ symmetry never prohibits the formation of the vertical earring EP ring (blue) in Fig. 3b.

In addition, we consider a vertical M_1 -symmetric loop $\Gamma_M = \hat{m}_1 \Gamma_M^{-1}$ enclosing \mathbf{K}_0 (the dashed green circle in Fig. 3a), where the negative exponent indicates the direction of the loop is reversed by reflection. Γ_M is demanded to cross Π_1 in two disconnected regions, A and B, of exact phases nearby the EC. As another prerequisite, the order of the $M_1-\dagger$ -parities of the two

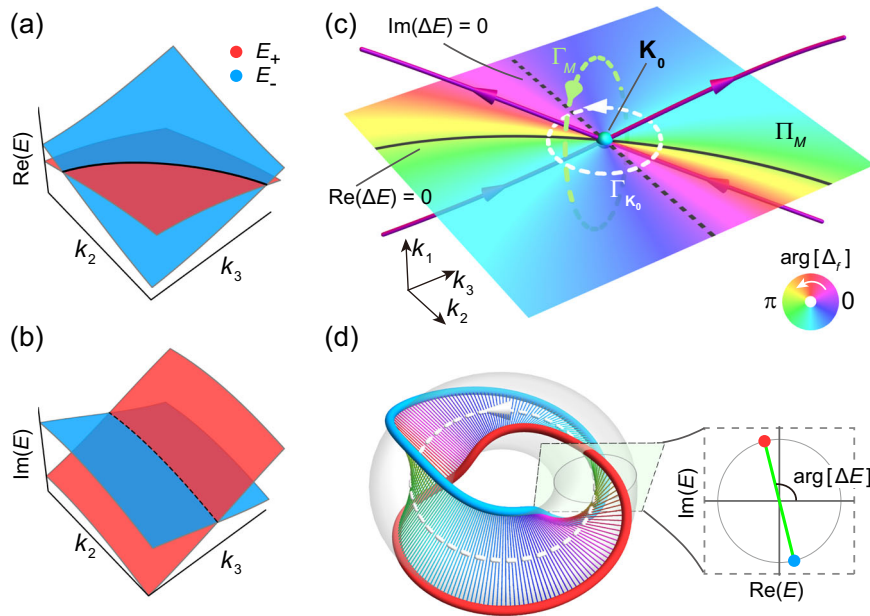


Fig. 4 Exceptional chain protected by mirror symmetry. **a, b** Real and imaginary parts of two bands E_+ , E_- with opposite mirror parities on the mirror plane Π_M . **c** Mirror-symmetric exceptional chain intersecting at \mathbf{K}_0 on Π_M . Colormap on Π_M : the phase vortex of $\Delta_f(\mathbf{k}_m)$ around \mathbf{K}_0 . **d** Eigenenergy braiding of E_+ (red), E_- (light blue) along the loop $\Gamma_{\mathbf{K}_0}$ encircling \mathbf{K}_0 forms a Hopf link with two rings of opposite mirror parities. Inset: section at a point $\mathbf{k}_0 \in \Gamma_{\mathbf{K}_0}$ gives $E_+(\mathbf{k}_0)$, $E_-(\mathbf{k}_0)$ on the complex plane. Color of the bar depicts $\arg[\Delta_f]$, which is twice as big as the bar's twist angle $\arg[\Delta E]$.

crossing bands must be reversed in the regions A and B , which means $\tilde{p}_A^+ \tilde{p}_B^+ = -1$, where the superscript “+” denotes the band with a larger real part of eigenenergy in each region. We will show later that if the planar EC is directly evolved from a mirror-symmetry-protected Hermitian nodal line, the opposite M_1 - \dagger -parities in regions A and B are guaranteed.

Despite having a null DN, the loop Γ_M carries a nontrivial Berry phase quantized by M_1 - \dagger symmetry, (see Methods and Supplementary Note 5):

$$\begin{aligned} & \exp[i\theta(\Gamma_M)] \\ &= \exp[i\text{Re}[\theta^{\text{LR}}(\Gamma_M)]] = \exp[i\text{Re}[\theta^{\text{RL}}(\Gamma_M)]] \\ &= \exp\left[i\frac{1}{2}(\theta^{\text{LL}}(\Gamma_M) + \theta^{\text{RR}})\right] = \tilde{p}_A^+ \tilde{p}_B^+ = -1, \end{aligned} \quad (10)$$

i.e., $\theta(\Gamma_M) = \pi \bmod 2\pi$, where $\theta^{\alpha\beta}(\Gamma_M) = \oint_{\Gamma_M} A^{\alpha\beta}(\mathbf{k}) \cdot d\mathbf{k}$ and $A^{\alpha\beta}(\mathbf{k}) = -i\langle \psi^\alpha(\mathbf{k}) | \nabla_{\mathbf{k}} | \psi^\beta(\mathbf{k}) \rangle$ ($\alpha, \beta \in \{L, R\}$) denote the four different types of Berry phases and Berry connections. And in computing A^{LL} and A^{RR} , the left and right eigenstates are required to obey the gauge constraint $\langle \psi^L(\mathbf{k}) | \psi^R(\mathbf{k}) \rangle \in \mathbb{R}$. Therefore, the nontrivial Berry phase along Γ_M ensures that the intersection of the ELs cannot be gapped out in the way that Fig. 3(c) shows, justifying the stability of the planar EC.

From the above analysis, we see that the stability of planar ECs comes from the joint protection of both eigenvalue-based (source-free principle of ELs) and eigenvector-based (quantized Berry phase) topological mechanisms. This explains why planar chains cannot stably exist in Hermitian systems, where only the eigenvectors contribute to the nontrivial topology.

Mirror-symmetric exceptional chains. The realization of M - \dagger or $C_2\mathcal{T}$ protected ECs relies on the confinement of ELs into symmetry-invariant planes. Next, we show that a single mirror symmetry can give rise to EC formation with all ELs leaving from high-symmetry planes, whose mechanism has no Hermitian counterpart.

For a general mirror-symmetric non-Hermitian system satisfying $\hat{M}\mathcal{H}(\hat{m}\mathbf{k})\hat{M}^{-1} = \mathcal{H}(\mathbf{k})$, every eigenstate on the mirror plane Π_M has a definite (even or odd) mirror-parity. Considering two bands with opposite M -parities on Π_M , their eigenenergies $E_+(\mathbf{k}_m)$, $E_-(\mathbf{k}_m)$, are well-ordered by the parities (see Fig. 4a, b), hence $\Delta E = E_+ - E_-$ is single-valued in the regions where no other band crosses. The intersection of the two bands on the mirror plane requires both the real and imaginary parts of the two eigenenergies to be equal, $\text{Re}[\Delta E(\mathbf{k}_m)] = 0$ and $\text{Im}[\Delta E(\mathbf{k}_m)] = 0$, which corresponds to two curves on Π_M with their crossing point (e.g., the cyan dot \mathbf{K}_0) determining the degeneracy of the two bands, as illustrated in Fig. 4c. Consequently, in contrast to the well-known fact that Hermitian band crossings on the mirror plane form nodal lines³, two non-Hermitian bands with opposite M -parities always stably intersect at isolated points inside the mirror plane. Moreover, since the eigenstates' coalescence is forbidden by their opposite M -parities, these isolated nodal points are non-defective, whereas an EP inside the mirror plane can only be formed by two bands with the same M -parity.

Indeed, the mirror-symmetry-protected nodal point \mathbf{K}_0 is a phase singularity of $\Delta E(\mathbf{k}_m)$. And since $\Delta E(\mathbf{k}_m)$ is single-valued near \mathbf{K}_0 , the energy vorticity of the two intersecting bands must take the integer value $\nu_{+-}(\Gamma_{\mathbf{K}_0}) = \frac{1}{2\pi} \oint_{\Gamma} d\arg[\Delta E] = \pm 1$ along any loop $\Gamma_{\mathbf{K}_0}$ (white dashed line) on Π_M solely encircling the degenerate point \mathbf{K}_0 . Thus, the DN of $\Gamma_{\mathbf{K}_0}$, which is entirely attributed to $\nu_{+-}(\Gamma_{\mathbf{K}_0})$, is quantized to an even number (see the phase vortex of $\Delta_f(\mathbf{k}_m)$ on Π_M in Fig. 4c)

$$\mathcal{D}(\Gamma_{\mathbf{K}_0}) = 2\nu_{+-}(\Gamma_{\mathbf{K}_0}) = \pm 2, \quad (11)$$

indicating the non-defective node \mathbf{K}_0 is an intersection of two ELs that pierce the mirror plane from the same side and form a mirror-symmetry-protected EC. Different from the M - \dagger or $C_2\mathcal{T}$ cases, the two crossing ELs are distributed antisymmetrically about Π_M , i.e., they have M -symmetric shapes but opposite orientations, as the consequence of $\mathcal{D}(\Gamma) = \mathcal{D}(\hat{m}\Gamma)$ for two mirror-partner loops imposed by the mirror symmetry (see Supplementary Note 3).

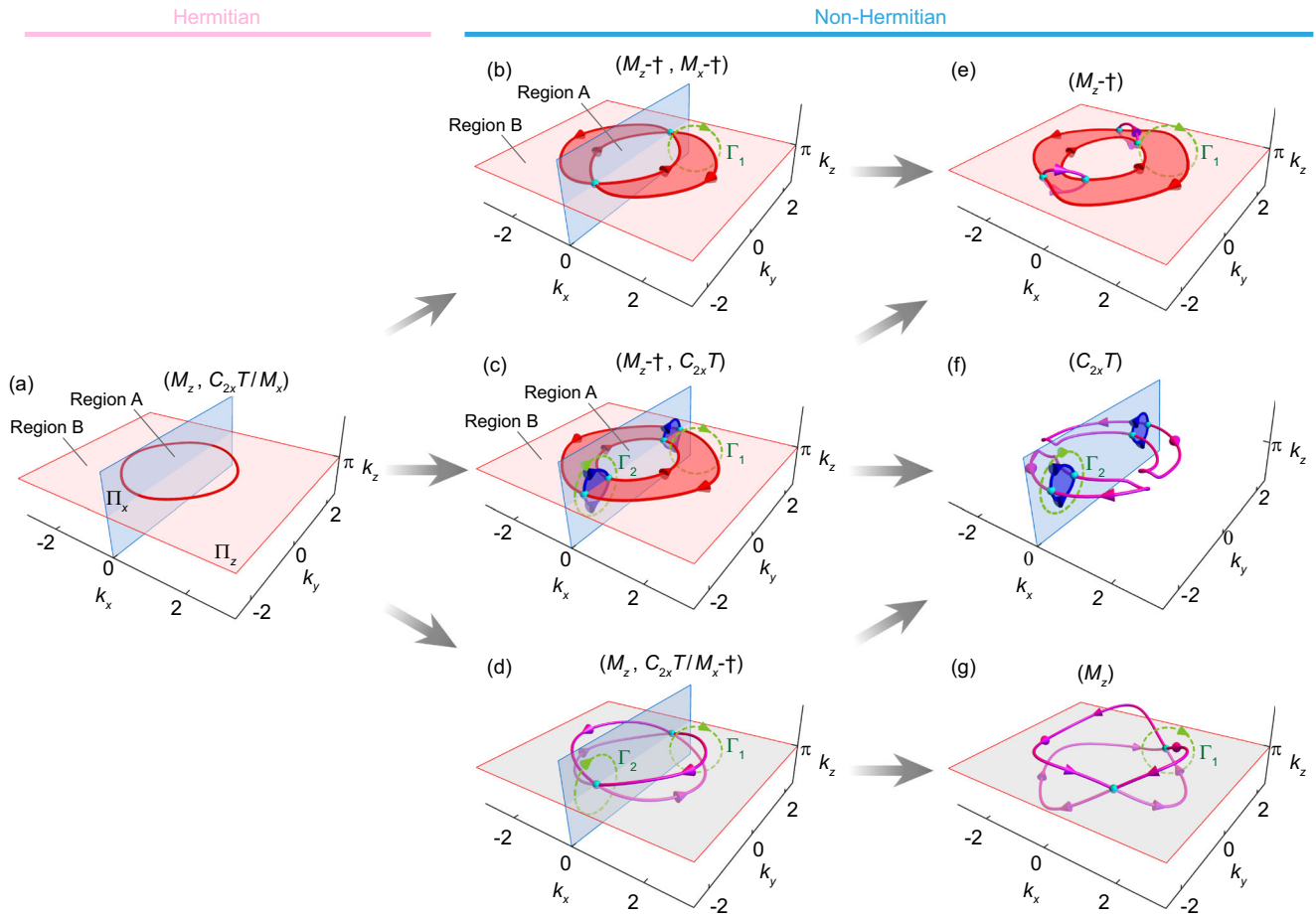


Fig. 5 Different types of exceptional chains (ECs) evolved from a nodal ring. **a** A Hermitian nodal ring protected by M_z symmetry lies on the mirror plane Π_z . A second symmetry of $C_{2x}\mathcal{T}$ or M_x presents with the corresponding high-symmetry plane Π_x . **b–d** ECs induced by non-Hermitian perturbation respecting two different symmetries, where the chain points (cyan dots) are fixed on the intersection line between Π_x and Π_z . **e–g** ECs protect by a single symmetry. The parenthesis above each configuration gives the required symmetries of that case. The Hamiltonians of all nodal structures are listed in Supplementary Table 4. Color scheme: A colored (red or blue) plane indicates the eigenstates can be classified into an exact (lighter region) or broken (darker region) phase on that plane, while a gray plane indicates exact and broken phases cannot be defined on it. Red, blue, and magenta tubes denote the exceptional lines lying on the $k_z = \pi$ plane, on the $k_x = 0$ plane, and out of any high-symmetry planes, respectively.

According to the relation Eq. (3), the DN $\mathcal{D}(\Gamma_{\mathbf{K}_0}) = \pm 2$ indicates that the two eigenmodes of opposite M -parities braid twice along the loop $\Gamma_{\mathbf{K}_0}$. Therefore, when returning to the initial states after a round, their eigenenergy trajectories are interwoven into a mirror-symmetry-protected Hopf link^{33,36}. As shown in Fig. 4d, the colored bars connecting the two trajectories represent the vector $\Delta\vec{E}(\mathbf{k}_\theta) = (\text{Re}[\Delta E], \text{Im}[\Delta E])$ ($\mathbf{k}_\theta \in \Gamma_{\mathbf{K}_0}$) on the complex energy plane, whose altitude angle gives $\arg[\Delta E]$. Therefore, the eigenenergy Hopf link delineates the twist of the vector $\Delta\vec{E}$ around the loop.

Meanwhile, for the M -symmetric loop Γ_M (dashed green circle in Fig. 4c) vertically circumnavigating the chain point \mathbf{K}_0 , the mirror symmetry also guarantees the nontrivial quantization of all four types of Berry phases along Γ_M (see Methods and Supplementary Note 5):

$$\theta^{LL}(\Gamma_M) = \theta^{RR}(\Gamma_M) = \theta^{LR}(\Gamma_M) = \theta^{RL}(\Gamma_M) = \pi \text{ mod } 2\pi. \quad (12)$$

Therefore, akin to the planar ECs, the stability of the mirror-symmetric EC also stems from the combined protection of the eigenvalue-induced and eigenvector-induced topological charges along the loops $\Gamma_{\mathbf{K}_0}$ and Γ_M , which prohibit the two intersecting ELs from disconnecting along k_1 and k_2 directions, respectively.

Exceptional chains arising from a nodal ring. In the previous sections, we have introduced three DAS symmetries, M , M - \dagger , $C_2\mathcal{T}$, and M , that can protect ECs. Here, starting from an M_z -protected Hermitian nodal ring (Fig. 5a) in the mirror plane Π_z (light red), we will enumerate all possible EC structures that can be deterministically generated by thresholdless non-Hermitian perturbations preserving M , M - \dagger or $C_2\mathcal{T}$ symmetries.

We first introduce M_z - \dagger -invariant non-Hermitian perturbations. As shown in Fig. 5b, c, since the system becomes pseudo-Hermitian on Π_z , the nodal line immediately splits into a pair of ELs confined in Π_z . Considering an M_z -symmetric loop Γ_1 around the EL pair, it carries a zero DN, $\mathcal{D}(\Gamma_1) = 0$, inherited from the Hermitian system. Meanwhile, the M_z - \dagger -parities of the two crossing bands in the regions, A and B, of exact phase are also inherited from the M_z -parities in the Hermitian case in Fig. 5a. The original M_z -parities of the two Hermitian bands take opposite orders in the two regions. This ensures the inherited non-Hermitian M_z - \dagger -parities in the two regions (Fig. 5b, c) satisfy $\tilde{p}_A^+ \tilde{p}_B^+ = -1$ and hence the quantized biorthogonal Berry phase along Γ_1 is nontrivial $\theta(\Gamma_1) = \pi$ (see Eq. (12)). The null DN and nontrivial Berry phase along Γ_1 oblige the two ELs to be oppositely directed but exempt from pair annihilation.

If the system under non-Hermitian perturbations also preserves a second symmetry $R_2 \in \{C_{2x}\mathcal{T}, M_x - \dagger\}$ with an

R_2 -invariant plane, Π_x , normally crossing Π_z , the EL pair in Π_z should reverse their directions when traversing Π_x , then two different types of ECs can be deterministically formed. When $R_2 = M_x - \dagger$, evolving from the M_x symmetry of the Hermitian case, the absence of nodal lines in Π_x in Fig. 5a indicates the two original Hermitian bands share the same M_x -parity. So an identical $M_x - \dagger$ -parity is inherited by the two non-Hermitian bands in Π_x . According to our analysis in Fig. 3, this identical $M_x - \dagger$ -parity protects the two ELs in Π_z robustly intersect at two non-defective chain points (cyan dots) when they cross Π_x , as shown in Fig. 5b, therefore forming a planar EC. If the $M_x - \dagger$ symmetry is broken, the ban on EPs appearing in Π_x is lifted; then as shown in Fig. 5e, each non-defective chain point spawns a vertical EP ring lying out of high-symmetry planes at once. Intriguingly, the vertical EP rings remain connected with the planar ELs in Π_z , and the EC survives. This remarkable robustness of EC is because the directions of the ELs cannot change abruptly and the source-free requirement (Eq. (5)) at the direction-reversal points of the in-plane ELs compels the emergence of the out-of-plane ELs from those points, uncovering that the $M_z - \dagger$ symmetry itself can stabilize ECs.

When $R_2 = C_{2x}\mathcal{T}$, the non-Hermitian perturbation expands the intersection points between the Hermitian nodal line and the plane Π_x into two exceptional rings (blue) fixed in Π_x bridging the gaps between the pair of ELs in Π_z (see Fig. 5c), akin to the formation of an exceptional ring from a Dirac point in 2D \mathcal{PT} symmetric systems (similar to Fig. 3b)^{8,82,83}. Thus, a double-earring EC can be realized. In addition, if the $M_z - \dagger$ symmetry is broken while $C_{2x}\mathcal{T}$ persists as shown in Fig. 5f, a $C_{2x}\mathcal{T}$ -protected π -quantized biorthogonal Berry phase, $\theta^{\text{LR}} = \oint_{\Gamma_2} A^{\text{LR}}(\mathbf{k}) \cdot d\mathbf{k} = \pi$, along a loop Γ_2 in Π_x protects the earring exceptional ring against shrinking to disappear (see Methods), and the EC stays alive in the presence of only the $C_{2x}\mathcal{T}$ symmetry. However, since the annihilation between the two horizontal ELs is now permissible in that the biorthogonal Berry phase $\theta(\Gamma_1)$ is no longer quantized, the EC can split into two separate ones shown by Fig. 5f.

Next, we consider the case in which the introduced non-Hermitian perturbation preserves the M_z symmetry. As exhibited in Fig. 5d, g, the nodal line splits into two ELs antisymmetrically distributed at the two sides of Π_z . Provided that the two ELs meet inside the mirror plane, M_z symmetry can protect their stable intersections at non-defective diabolic points on Π_z and hence guarantees the formation of EC, as illustrated in the above section. By imposing another symmetry $R_2 \in \{C_{2x}\mathcal{T}, M_x - \dagger\}$, the chain point can be further fixed on the intersection line of the two planes Π_x and Π_z by the DAS point group $m_2 m_x^\dagger 2_y^\dagger$ or $2'_x m_y m_z$ (see Supplementary Note 6). Breaking R_2 while preserving M_z , the chain points can move freely in the M_z -invariant plane Π_z , as shown in Fig. 5g, which cannot disappear unless annihilating in pairs of opposite DN $\mathcal{D} = \pm 2$. Conversely, if we break M_z while maintaining $R_2 = C_{2x}\mathcal{T}$, the M_z -symmetric EC in Fig. 5d can evolve to the configuration in Fig. 5f.

The concrete Hamiltonians generating the ECs in Fig. 5 are given in Supplementary Note 6, where we also offer a rigorous analysis of the determinate evolution paths toward various local morphologies of ECs from a DAS point group perspective. Furthermore, if we break the symmetries protecting the chain points in certain manners, the ECs can also deterministically evolve into more fascinating exceptional links^{45,46,69} (see details in Supplementary Note 7). As a result, ECs can be used as critical phases for producing exceptional links in non-Hermitian crystals.

Photonic crystal realization of exceptional chains. In this section, we will show that various types of ECs protected by different DAS crystalline symmetries can be realized in non-Hermitian

photonic crystals. It has been experimentally proved that a Hermitian metallic-mesh PC supports nodal chains protected by both \mathcal{PT} symmetry and three mirror symmetries $M_{x,y,z}$ ⁵⁸, and the nodal rings on different mirror planes can be expanded into exceptional torus if \mathcal{PT} -symmetric non-Hermiticity is introduced⁸⁴. Here, we first modify the metallic mesh PC so as to design a prototypical non-Hermitian PC with three mirror-adjoint symmetries. One thing to note is that a reciprocal PC with the three $M_{x,y,z} - \dagger$ symmetries must be \mathcal{PT} symmetric, inasmuch as reciprocity is equivalent to the time-reversal-adjoint symmetry, $T - \dagger$ ¹², and $(M_x - \dagger)(M_y - \dagger)(M_z - \dagger)(T - \dagger) = \mathcal{PT}$. Therefore, to realize ELs on the mirror planes in all three directions instead of EP surfaces, we need to break the \mathcal{PT} symmetry and accordingly the reciprocity of the PC, which can be achieved by properly arranging the non-Hermitian gyrotropic materials with the relative permittivity and permeability surrounding the metallic mesh:

$$\varepsilon_r(\mathbf{r}) = \begin{pmatrix} 1 + i\gamma(\mathbf{r}) & i\alpha(\mathbf{r}) & 0 \\ -i\alpha(\mathbf{r}) & 1 + i\gamma(\mathbf{r}) & 0 \\ 0 & 0 & 1 + i\gamma(\mathbf{r}) \end{pmatrix}, \mu_r = 1, \quad (13)$$

where $\alpha(\mathbf{r})$ and $\gamma(\mathbf{r})$ are real-valued functions of coordinates, characterizing, respectively, the distributions of gyrotropy and loss-gain in the background materials.

Figure 6a displays the non-reciprocal Hermitian metallic mesh PC with $\gamma = 0$, where the prism regions are magnetized with the red (blue) arrows denoting the gyration vectors corresponding to $\alpha = 0.5$ (-0.5). The Hermitian space group of the PC is $Pmmm1^\dagger$ (No. 1698⁷²) including three mirror symmetries, $M_{x,y,z}$, but no \mathcal{PT} symmetry. Figure 6d shows the bulk band structure of the Hermitian PC along high symmetry lines (see Fig. 6g), which is numerically calculated by the commercial software COMSOL Multiphysics. Since the two bands near the frequency of $f = 0.65c/a$ (light-blue region) have opposite mirror parities (labels on the band structure) along every intersection line of two orthogonal mirror planes, as shown in Fig. 6g-i, the nodal rings in different mirror planes should connect together^{56,57,63} and form a globally connected nodal chain network, where the nodal rings are retrieved from the 2D band structure on the mirror planes (see Supplementary Note 10). For the lower two bands at about $f = 0.6c/a$ (light-pink region) with opposite M_z parities but identical $M_{x,y}$ parities, the nodal ring only appears on the $k_z = \pi/a$ plane, as shown by Fig. 6g-ii.

Introducing loss (gain) with $\gamma = 0.5$ (-0.5) into the background materials in red (cyan) color in Fig. 6b, the prototype Hermitian PC becomes non-Hermitian and the three mirror symmetries $M_{x,y,z}$ convert to the corresponding mirror-adjoint symmetries, $M_{x,y,z} - \dagger$, so the DAS space group of the PC becomes $Pm\bar{1}m^\dagger m^\dagger$ (No. 3558⁷²). The non-Hermitian perturbed band structure is plotted in Fig. 6e. The nodal rings in different mirror planes are split into paired exceptional rings with opposite orientations. For the upper pair of bands near $f = 0.65c/a$, the two EP rings on each plane can be marked as “inner” and “outer” according to their relative positions. In particular, every inner (outer) EP ring on a mirror plane is chained with another two outer (inner) rings in the two perpendicular planes, resulting in a pair of triply orthogonal EC networks linked with each other (see the tight-binding model generating the same EC structure in Supplementary Note 8), as depicted by Fig. 6h-i. Moreover, the numerical tests also verify that the numbers of inflow and outflow ELs at each chain point are balanced (see Supplementary Note 10), corroborating the source-free principle of ELs. The multi-band nature of the PC also demonstrates that our theory of EC formation is universal for generic full-wave crystalline systems.

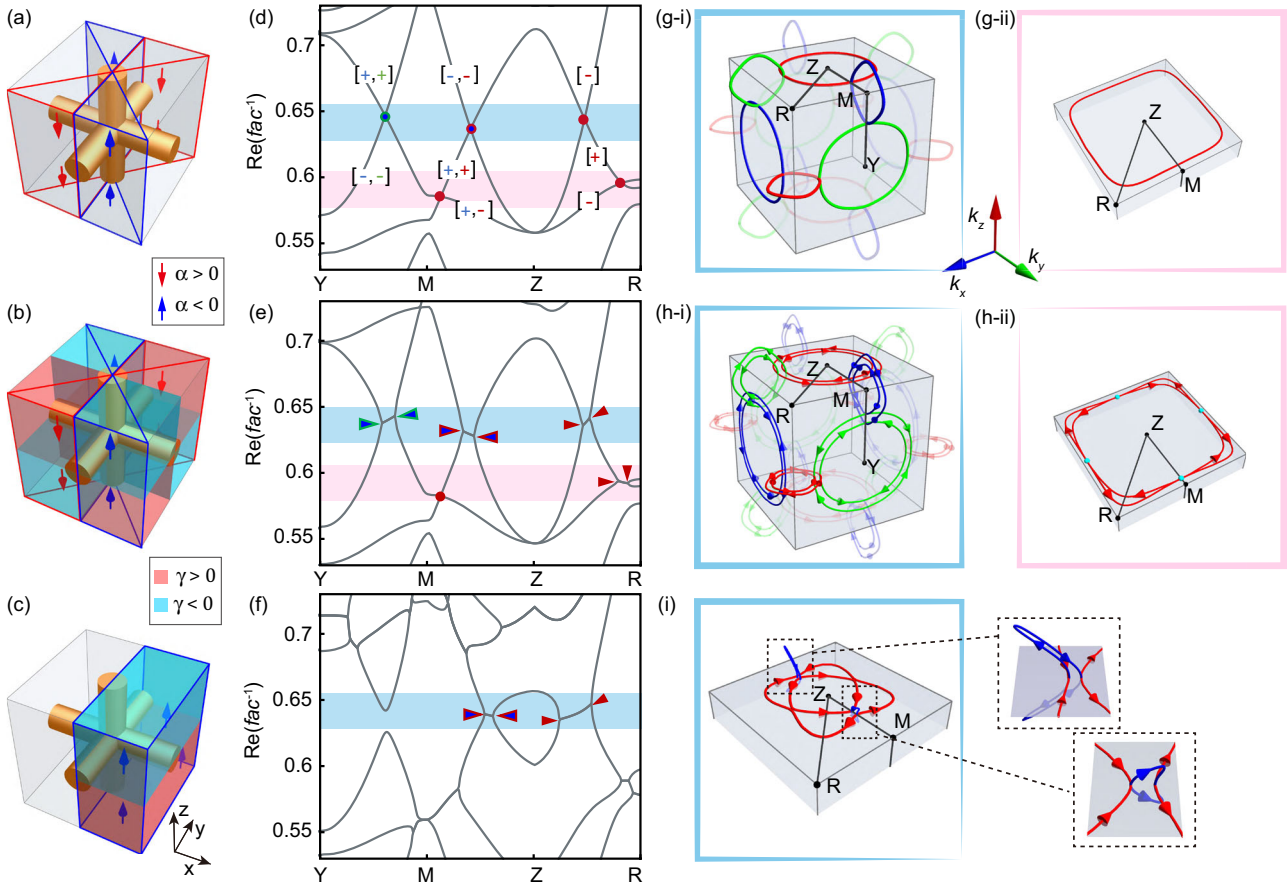


Fig. 6 Different types of exceptional chains (ECs) in non-Hermitian photonic crystals (PCs). **a, b, c** Schematics of three cubic PCs' unit cells with lattice constant a . Orange cylinders: metallic meshes. Regions in gray, red, and cyan colors: conservative ($\gamma = 0$), lossy ($\gamma > 0$), and gain ($\gamma < 0$) materials, respectively. Regions with down-red (up-blue) arrows: gyrotropic media with $\alpha > 0$ ($\alpha < 0$). **d, e, f** Band structures (real part) along high symmetry lines Y-M-Z-R corresponding to the PCs in **(a, b, c)**. Triangles (dots) in blue, green, and red represent exceptional (diabolic) chain points. Two-tone triangles (dots) represent the exceptional (diabolic) chain points. **g, h, i** The nodal structures in the Brillouin zone of the PCs in **(a, b, c)**. **a, d, g** The Hermitian PC in **(a)** respecting $M_{x,y,z}$ symmetries with $\alpha = \pm 0.5$ and $\gamma = 0$. Labels $[\pm]$ in blue, green and red in **(d)**: the $M_{x,y,z}$ -parities of the bands, respectively. **g-i** Nodal chain formed around $f = 0.65c/a$ (light blue shaded region in **(d)**); **(g-ii)** Nodal ring formed around $f = 0.6c/a$ (pink shaded region in **(d)**). **b, e, h** The non-Hermitian PC respecting $M_{x,y,z}-\dagger$ symmetries with $\alpha = \pm 0.5$, $\gamma = \pm 0.5$. **h-i** A pair of linked orthogonal EC network formed around $f = 0.65c/a$ (light blue shaded region in **(e)**); **(h-ii)** A planar EC with four non-defective chain points (cyan dots) formed around $f = 0.6c/a$ (pink shaded region in **(e)**). **c, f, i** The non-Hermitian PC respecting $M_z-\dagger$ and $C_{2x}\mathcal{T}$ symmetries with $\alpha = -0.3$, $\gamma = \pm 0.5$. **i** A double-earring EC formed around $f = 0.65c/a$ (light blue shaded region in **(f)**).

For the lower pair of bands around $f = 0.6c/a$, thanks to their identical $M_x-\dagger$ ($M_y-\dagger$) parity on the mirror plane of $k_x = 0$ ($k_y = 0$) inherited from the Hermitian mirror parity, the Hermitian degenerate points of the two bands along $k_x = 0$ (M-Z direction in Fig. 6d) stay intact after introducing the non-Hermiticity (Fig. 6e), and so do the Hermitian degenerate points along $k_y = 0$. Consequently, as seen from Fig. 6h-ii, the pair of exceptional rings splitting from the Hermitian nodal ring intersect at four $M_{x,y}-\dagger$ -protected non-defective diabolic points (cyan) and therefore form a planar EC in the $k_z = \pi/a$ plane.

In the last row of Fig. 6, we designed another metallic mesh PC with a different distribution of the gyrotropic and nonconservative materials (see the unit cell in Fig. 6c and the band structure in Fig. 6f), such that its space group is $Pm\bar{1}m'2'$ (No. 8967) possessing $M_z-\dagger$ and $C_{2x}\mathcal{T}$ symmetries. Because of the lack of $M_{x,y}$ symmetries in the prototype Hermitian PC ($\gamma = 0$), only the M_z -invariant planes can support Hermitian nodal rings in this case. After bringing gain and loss into the PC, the nodal ring in the $k_z = \pi/a$ plane divides into two planar exceptional rings (red) joining together by two vertical EP loops (blue) in the $k_x = 0$ plane protected by the $C_{2x}\mathcal{T}$ symmetry, as can be seen from

Fig. 6i. As a result, a double-earring EC arises in the non-Hermitian PC, reproducing the configuration in Fig. 5c.

Discussion

In conclusion, we established the source-free principle of directed ELs and showed that the source-free principle together with symmetry constraints are two crucial conditions for the formation of ECs. Based on this idea, we developed a general theory for constructing ECs of various local morphologies, including orthogonal EC, planar EC, and mirror-symmetric EC, protected by $C_2\mathcal{T}$, mirror-adjoint, or mirror symmetries. We also investigated all possible EC configurations evolving from a Hermitian nodal ring with thresholdless non-Hermitian perturbations. To further illustrate the idea, we designed non-Hermitian PCs respecting certain symmetries that exhibit three representative and exotic ECs in the PCs, i.e., a pair of linked orthogonal EC networks, a planar EC with non-defective chain points, and a double-earring EC. It is worth emphasizing that the source-free principle of ELs and symmetry constraints not only account for the formation of two-band ECs but are also applicable to

multiband cases, such as the exceptional nexus of the ELs formed by the intersections of triple bands⁶¹ (see Supplementary Note 9).

Compared with Hermitian nodal chains, the morphologies of ECs exhibit richer diversities. Both the planar EC and mirror-symmetric EC have no Hermitian analogs. And their stability stems from the combined protection of eigenvalue-based and eigenvector-based topological mechanisms, which goes beyond the protection granted by only a single type of topological invariant defined by eigenvectors (quantized Berry phase or winding number) in Hermitian nodal chains. In particular, the various formation mechanisms of ECs lead to different types of degeneracy at the chain points of ECs, including the ordinary second-order exceptional chain points in orthogonal ECs, the non-defective diabolic chain points in planar and mirror-symmetric ECs, or even the higher-order exceptional chain points in multiband ECs (see Supplementary Note 9). The variety of degeneracies at the chain points also suggests that different types of ECs may produce remarkably different transport or excitation effects, which would be useful for direction-sensitive sensing and anisotropic spontaneous emission enhancement.

Our theory integrates the non-Hermitian topology with the DAS crystalline symmetries and opens the avenue for symmetry-protected non-Hermitian topological phases and topological degeneracies, such as symmetry-protected higher-order EPs^{85–88}, in non-Hermitian crystals. In light of the analogy between non-Hermitian physics and other systems or theories^{89–91}, our framework may also be transplanted to these systems, giving rise to exotic physical effects. For example, it was recently discovered that the circular polarization singularity (C point) of 3D optical polarization fields can map to a non-Hermitian EP⁹¹. Therefore, the present method would also be applied to realize symmetry-protected chains of C points for 3D optical fields in the real space.

Methods

Non-Hermitian crystalline symmetries and DAS space groups. An anti-symmetry A with respect to a group \mathcal{G} is defined as an operator satisfying three conditions⁷¹:

	1	1'	1†	1‡
1	1	1'	1†	1‡
1'	1'	1	1‡	1†
1†	1†	1‡	1	1'
1‡	1‡	1†	1'	1

Fig. 7 Multiplication table of the three antisymmetry operations. Here, 1, 1', 1†, 1‡ are the generalized Hermann-Mauguin notations of the identity, time reversal, Hermitian-adjoint, and reciprocity transformations, respectively.

1. A itself is not an element of \mathcal{G} : $A \notin \mathcal{G}$;
2. Involutivity (self-inverseness): $A^2 = I$;
3. A commutes with all elements of \mathcal{G} : $[A, G] = 0, \forall G \in \mathcal{G}$.

For example, the time reversal operator \mathcal{T} (1' in HM notation) is an antisymmetry for spinless space (point) groups, hence involving \mathcal{T} into the crystallographic space (point) groups gives rise to single-antisymmetry space (point) groups, i.e., the magnetic space (point) groups.

For non-Hermitian systems, the Hermitian-adjoint operation has been shown to be a new symmetry dimension that can greatly enrich the non-Hermitian topological phases¹². In contrast to the spatiotemporal transformations which are linear (antilinear) operators acting on the states in Hilbert space, the Hermitian-adjoint (1† in HM notation) is an antiautomorphic map on the set of bounded linear operators (mathematically, a noncommutative ring) on the Hilbert space. Nevertheless, the spatiotemporal transformations, say G , may also be regarded as maps between linear operators via unitary transformation:

$G(\mathcal{H}) = \hat{G}\mathcal{H}\hat{G}^{-1} = \hat{G}\mathcal{H}\hat{G}^\dagger$. In this sense, the Hermitian-adjoint map indeed manifests as an antisymmetry to any group \mathcal{G} of unitary transformations, since it is self-inverse $1^\dagger 1^\dagger(\mathcal{H}) = (\mathcal{H}^\dagger)^\dagger = \mathcal{H}$ and commutative with any unitary

transformation $1^\dagger G(\mathcal{H}) = (\hat{G}\mathcal{H}\hat{G}^\dagger)^\dagger = \hat{G}\mathcal{H}^\dagger\hat{G}^\dagger = G1^\dagger(\mathcal{H}), \forall G \in \mathcal{G}$.

Consequently, by taking both time-reversal 1' and Hermitian-adjoint 1† into account, we find that the expanded space (point) group for a non-Hermitian crystal is generally isomorphic to a double-antisymmetry space (point) group⁷². In particular, the product of time-reversal and Hermitian-adjoint operations (denoted 1‡ in HM notation) is also an antisymmetry to space groups. Physically, it just represents the reciprocity transformation, $\mathcal{T} - \dagger$, of the system¹². These three antisymmetry operations together with identity transformation constitute a group isomorphic to the dihedral group D_2 with the multiplication table shown in Fig. 7.

In the DAS space (point) groups for non-Hermitian crystals, the symmetries are sorted into four types:

- (i) The pure spatial symmetries, denoted G or g :

$$\hat{G}\mathcal{H}(\hat{g}^{-1}\mathbf{x})\hat{G}^{-1} = \mathcal{H}(\mathbf{x});$$

- (ii) The spatial-adjoint symmetries, denoted $G - \dagger$ or g^\dagger :

$$\hat{G}\mathcal{H}(\hat{g}^{-1}\mathbf{x})\hat{G}^{-1} = \mathcal{H}(\mathbf{x});$$

- (iii) The spatiotemporal symmetries, denoted GT or g' :

$$\hat{G}\hat{T}\mathcal{H}(\hat{g}^{-1}\mathbf{x})^*(\hat{G}\hat{T})^{-1} = \mathcal{H}(\mathbf{x});$$

- (iv) The spatiotemporal-adjoint symmetries, denoted $GT - \dagger$ or g'^\dagger :

$$\hat{G}\hat{T}\mathcal{H}(\hat{g}^{-1}\mathbf{x})^\dagger(\hat{G}\hat{T})^{-1} = \mathcal{H}(\mathbf{x}).$$

Here, $\hat{g} = \{R | \mathbf{w}\}$ denotes the spatial transformation, with a rotation part R and a translation part \mathbf{w} , acting on the position vector \mathbf{x} , and \hat{G}, \hat{T} denote the unitary parts associated with the G, T operators, respectively, acting on the internal degrees of freedom. The last three types of symmetries can be viewed as coloring the original space-group symmetries into red, blue, and green, respectively, so we can use colored symbols, i.e., $g^\dagger, g',$ and g'^\dagger , to represent these symmetries in the generalized HM notation (cf. the colored symbols in Fig. 7). And the DAS space (point) groups are obtained by coloring the elements of the original space (point) groups. There are 624 DAS point groups and 17803 DAS space groups in total^{70–72}.

Based on these four types of symmetries, the DAS space (point) groups can be classified into 12 categories⁷². In the table of Fig. 8, we list the 12 categories with assigning a physics meaningful designation to each category. The first category (1) includes all the original colorblind space groups \mathbf{Q} without any colored symmetries. The second column of the table shows four categories of gray space groups (namely, all elements in a group are uniformly colored), each of which possesses at

	Gray space groups	Single-antisymmetry groups	Multicolor groups
Colorless crystallographic space groups \mathbf{Q} Category (1)	TRS gray groups $\mathbf{Q}1'$ Category (2)	Magnetic groups \mathbf{Q}' Category (3)	TRS adjoint group $\mathbf{Q}^\dagger 1' = \mathbf{Q}'^\dagger 1'$ Category (9)
	Hermitian gray groups $\mathbf{Q}1^\dagger$ Category (4)	Adjoint groups \mathbf{Q}^\dagger Category (7)	Hermitian magnetic groups $\mathbf{Q}'^\dagger 1^\dagger = \mathbf{Q}'^\dagger 1^\dagger$ Category (6)
	Reciprocal gray groups $\mathbf{Q}1^\ddagger$ Category (8)	Magnetic-adjoint groups \mathbf{Q}^\ddagger Category (11)	Reciprocal magnetic groups $\mathbf{Q}'^\ddagger 1^\ddagger = \mathbf{Q}'^\ddagger 1^\ddagger$ Category (10)
	Hermitian -TRS groups $\mathbf{Q}1'1^\dagger$ Category (5)		Indecomposable DAS groups $\mathbf{Q}^{(\ddagger)\dagger}$ Category (12)

Fig. 8 Classification of double-antisymmetry space (point) groups for non-Hermitian crystals. The serial number (#) of each category listed in the table follows ref. 72.

Table 1 Quantized Berry phases of a self-closed band along a loop Γ protected by different types of twofold DAS point-group symmetries G .

Symmetry type	Loop	Other conditions	Quantized Berry phases (O or π mod 2π)	Examples
G	$\Gamma = \hat{g}\Gamma^{-1}$	none	$\theta^{LR} = \theta^{RL} = \theta^{LL} = \theta^{RR} = \arg(p(O)p(\pi))$	\mathcal{P}, M
$G-\dagger$	$\Gamma = \hat{g}\Gamma^{-1}$	two intersections of Γ and Π_G are in the exact phase	$\text{Re}[\theta^{LR}] = \text{Re}[\theta^{RL}] = \frac{1}{2}(\theta^{LL} + \theta^{RR}) = \arg(\tilde{p}(O)\tilde{p}(\pi))$	$M-\dagger$
GT	$\Gamma = -\hat{g}\Gamma$	Γ is in the exact phase	$\text{Re}[\theta^{LR}] = \text{Re}[\theta^{RL}] = \theta^{LL} = \theta^{RR}$	\mathcal{PT}, C_2T
$GT - \dagger$	$\Gamma = -\hat{g}\Gamma$	none	$\theta^{LR} = \theta^{RL} = \frac{1}{2}(\theta^{LL} + \theta^{RR})$	$\mathcal{PT} - \dagger$

The corresponding G -invariant subspace is $\Pi_G = \{\mathbf{k}_G | \hat{G}\mathbf{k}_G = \mathbf{k}_G\}$. $p(\phi) \in \{\pm 1\}$ and $\tilde{p}(\phi) \in \{\pm 1\}$ denote the G -parities and $G-\dagger$ -parities, respectively, of the eigenstates at the G -invariant points $\mathbf{k}(\phi)$ ($\phi \in [0, \pi]$).

least one antisymmetry, describing the time-reversal symmetric (TRS) systems, Hermitian systems, reciprocal systems, and Hermitian TRS systems, respectively. The third column shows the three categories of single-antisymmetry groups. For example, the groups in category (3) are just the black-white magnetic groups which only contain symmetries of types (i) and (iii) but do not have TRS. Similarly, in category (4), an adjoint group describes the non-Hermitian systems only possessing symmetries of types (i) and (ii). The space group of the PC shown in Fig. 6b, $Pm^{\dagger}m^{\dagger}m^{\dagger}$, just belongs to this category. The categories in the fourth column describe the groups containing at least three types of symmetries. In categories (6), (9), and (10), each group also contains an antisymmetry, contrary to the indecomposable groups in category (12) that violate all the three antisymmetries. For example, the space group of the PC shown in Fig. 6c, $Pm^{\dagger}m^{\dagger}2'$, belongs to the category (12).

Quantized Berry phases protected by DAS point-group symmetries. The quantization conditions for Berry phases protected by purely spatial and spatio-temporal point-group symmetries, such as \mathcal{PT} and mirror symmetries, have been widely investigated in Hermitian systems. However, when extending our perspective to non-Hermitian crystalline systems, we urgently need to test whether the results established in the Hermitian case still hold and whether the DAS point-group symmetries that are intrinsically non-Hermitian can also preserve the quantized Berry phases.

Moreover, since the left and right eigenvectors of the same eigenstate become different in non-Hermitian systems, more variants of Berry phases can be introduced, making the situation more complicated. Apart from the global biorthogonal Berry phase Θ in Eq. (4), we can define four different types of Berry phases, $\theta^{LL}(\Gamma)$, $\theta^{RR}(\Gamma)$, $\theta^{LR}(\Gamma)$, $\theta^{RL}(\Gamma)$, of a single continuous band along a loop $\Gamma = \{\mathbf{k}(\phi) | \mathbf{k}(\pi) = \mathbf{k}(-\pi), -\pi \leq \phi \leq \pi\}$ through integrating the corresponding Berry connections, $A^{LL}, A^{RR}, A^{LR}, A^{RL}$ ¹⁰.

$$\theta^{\alpha\beta}(\Gamma) = \oint_{\Gamma} d\mathbf{k} \cdot A^{\alpha\beta}(\mathbf{k}), \quad (14)$$

$$A^{\alpha\beta}(\mathbf{k}) = -i\langle \psi_n^{\alpha}(\mathbf{k}) | \nabla_{\mathbf{k}} | \psi_n^{\beta}(\mathbf{k}) \rangle, \quad (\alpha, \beta \in \{L, R\}), \quad (15)$$

where the eigenvectors $|\psi_n^{\alpha/\beta}(\mathbf{k})\rangle$ should be normalized by $\langle \psi_n^{\alpha}(\mathbf{k}) | \psi_n^{\beta}(\mathbf{k}) \rangle = 1$, which is dependent on the different α, β . For the biorthogonal Berry connections ($\alpha \neq \beta$), A^{LR}, A^{RL} , $|\psi_n^{\alpha/\beta}(\mathbf{k})\rangle$ respects the binormalization condition $\langle \psi_n^{\alpha}(\mathbf{k}) | \psi_n^{\beta}(\mathbf{k}) \rangle = 1$. Whereas for left or right Berry connections ($\alpha = \beta \in \{L, R\}$), A^{LL}, A^{RR} , $|\psi_n^{\alpha}(\mathbf{k})\rangle$ is just self-normalized: $\langle \psi_n^{\alpha}(\mathbf{k}) | \psi_n^{\alpha}(\mathbf{k}) \rangle = 1$.

The eigenstates along the loop Γ , abbreviated as $|\psi_n^{R/L}(\phi)\rangle := |\psi_n^{R/L}(\mathbf{k}(\phi))\rangle$, form a continuous band from $\phi = -\pi$ to π . To guarantee the Berry phases are well-defined, namely, the results are identical in the sense of modulo 2π for any continuous gauge of the eigenvectors along Γ , we require that the continuous band concerned is self-closed, namely the eigenstate returns to the initial one, i.e., $|\psi_n^{\alpha}(\pi)\rangle = |\psi_n^{\alpha}(-\pi)\rangle$, after traveling on the concerned band along the loop one turn (ϕ evolves from $-\pi$ to π).

In addition, according to the relation $A^{\alpha\beta*} = A^{\alpha\beta\dagger} = i\langle \nabla_{\mathbf{k}} \psi_n^{\beta} | \psi_n^{\alpha} \rangle = -i\langle \psi_n^{\beta} | \nabla_{\mathbf{k}} \psi_n^{\alpha} \rangle = A^{\beta\alpha}$, the two biorthogonal Berry connections, as well as the two biorthogonal Berry phases, are always complex-conjugate

$$A^{LR}(\mathbf{k}) = A^{RL}(\mathbf{k})^*, \quad \theta^{LR}(\Gamma) = \theta^{RL}(\Gamma)^*, \quad (16)$$

while the ordinary Berry connections and Berry phases for left (right) eigenvectors always take real values

$$A^{LL}(\mathbf{k}), A^{RR}(\mathbf{k}) \in \mathbb{R}^3, \quad \theta^{LL}(\Gamma), \theta^{RR}(\Gamma) \in \mathbb{R}. \quad (17)$$

In Supplementary Note 5, we proved that the four types of two-fold DAS point-group symmetries could protect the quantization of different kinds of Berry phases along symmetry-invariant loops, as summarized in Table 1. Here, two-fold symmetry means that $G^2 = I$. In computing $\frac{1}{2}(\theta^{LL} + \theta^{RR})$, the left and right eigenstates are required to satisfy the gauge constraint that $\langle \psi^L(\mathbf{k}) | \psi^R(\mathbf{k}) \rangle$ takes positive real values. In the Supplementary Information, we also showed that the

self-closeness of the band can be guaranteed by some rather lenient properties of the bands in each case.

Data availability

The data of simulations that support the findings of this study are available in DataSpace@HKUST with the identifier "<https://doi.org/10.14711/dataset/KKRJPL>"⁹².

Code availability

The code used to evaluate the conclusions in the paper is available upon request. Please contact the corresponding author.

Received: 4 May 2023; Accepted: 27 June 2023;

Published online: 08 July 2023

References

- Armitage, N. P., Mele, E. J. & Vishwanath, A. Weyl and Dirac semimetals in three-dimensional solids. *Rev. Mod. Phys.* **90**, 015001 (2018).
- Hasan, M. Z. et al. Weyl, Dirac and high-fold chiral fermions in topological quantum matter. *Nat. Rev. Mater.* **6**, 784–803 (2021).
- Fang, C., Weng, H., Dai, X. & Fang, Z. Topological nodal line semimetals. *Chin. Phys. B* **25**, 117106 (2016).
- Park, H., Gao, W., Zhang, X. & Oh, S. S. Nodal lines in momentum space: Topological invariants and recent realizations in photonic and other systems. *Nanophotonics* **11**, 2192–8614 (2022).
- Miđya, B., Zhao, H. & Feng, L. Non-Hermitian photonics promises exceptional topology of light. *Nat. Commun.* **9**, 1–4 (2018).
- Miri, M.-A. & Alù, A. Exceptional points in optics and photonics. *Science* **363**, aar7709 (2019).
- Özdemir, Ş. K., Rotter, S., Nori, F. & Yang, L. Parity-time symmetry and exceptional points in photonics. *Nat. Mater.* **18**, 783–798 (2019).
- Zhen, B. et al. Spawning rings of exceptional points out of Dirac cones. *Nature* **525**, 354–358 (2015).
- Cui, X., Ding, K., Dong, J.-W. & Chan, C. T. Realization of complex conjugate media using non-PT-symmetric photonic crystals. *Nanophotonics* **9**, 195–203 (2019).
- Shen, H., Zhen, B. & Fu, L. Topological band theory for non-Hermitian hamiltonians. *Phys. Rev. Lett.* **120**, 146402 (2018).
- Gong, Z. et al. Topological phases of non-Hermitian systems. *Phys. Rev. X* **8**, 031079 (2018).
- Kawabata, K., Shiozaki, K., Ueda, M. & Sato, M. Symmetry and topology in non-Hermitian physics. *Phys. Rev. X* **9**, 041015 (2019).
- Kawabata, K., Bessho, T. & Sato, M. Classification of exceptional points and non-Hermitian topological semimetals. *Phys. Rev. Lett.* **123**, 066405 (2019).
- Zhou, H. & Lee, J. Y. Periodic table for topological bands with non-Hermitian symmetries. *Phys. Rev. B* **99**, 235112 (2019).
- Li, L., Lee, C. H. & Gong, J. Geometric characterization of non-Hermitian topological systems through the singularity ring in pseudospin vector space. *Phys. Rev. B* **100**, 075403 (2019).
- Bergholtz, E. J., Budich, J. C. & Kunst, F. K. Exceptional topology of non-Hermitian systems. *Rev. Mod. Phys.* **93**, 015005 (2021).
- Heiss, W. D. Exceptional points of non-Hermitian operators. *J. Phys. A: Math. Gen.* **37**, 2455–2464 (2004).
- Ding, K., Ma, G., Xiao, M., Zhang, Z. Q. & Chan, C. T. Emergence, coalescence, and topological properties of multiple exceptional points and their experimental realization. *Phys. Rev. X* **6**, 021007 (2016).

19. Cui, X., Ding, K., Dong, J.-W. & Chan, C. T. Exceptional points and their coalescence of PT symmetric interface states in photonic crystals. *Phys. Rev. B* **100**, 115412 (2019).
20. Wiersig, J. Enhancing the sensitivity of frequency and energy splitting detection by using exceptional points: application to microcavity sensors for single-particle detection. *Phys. Rev. Lett.* **112**, 203901 (2014).
21. Hodaie, H. et al. Enhanced sensitivity at higher-order exceptional points. *Nature* **548**, 187–191 (2017).
22. Chen, W., Kaya Özdemir, Ş., Zhao, G., Wiersig, J. & Yang, L. Exceptional points enhance sensing in an optical microcavity. *Nature* **548**, 192–196 (2017).
23. Xiao, Z., Li, H., Kottos, T. & Alù, A. Enhanced sensing and nondegraded thermal noise performance based on PT-symmetric electronic circuits with a sixth-order exceptional point. *Phys. Rev. Lett.* **123**, 213901 (2019).
24. Gao, T. et al. Observation of non-Hermitian degeneracies in a chaotic exciton-polariton billiard. *Nature* **526**, 554–558 (2015).
25. Doppler, J. et al. Dynamically encircling an exceptional point for asymmetric mode switching. *Nature* **537**, 76–79 (2016).
26. Hassan, A. U., Zhen, B., Soljačić, M., Khajavikhan, M. & Christodoulides, D. N. Dynamically encircling exceptional points: exact evolution and polarization state conversion. *Phys. Rev. Lett.* **118**, 093002 (2017).
27. Zhang, X.-L., Wang, S., Hou, B. & Chan, C. T. Dynamically encircling exceptional points: in situ control of encircling loops and the role of the starting point. *Phys. Rev. X* **8**, 021066 (2018).
28. Peng, B. et al. Chiral modes and directional lasing at exceptional points. *Proc. Natl. Acad. Sci. USA* **113**, 6845–6850 (2016).
29. Miao, P. et al. Orbital angular momentum microlaser. *Science* **353**, 464–467 (2016).
30. Longhi, S. & Feng, L. Unidirectional lasing in semiconductor microring lasers at an exceptional point [Invited]. *Photon. Res.* **5**, B1–B6 (2017).
31. Wojcik, C. C., Sun, X.-Q., Bzdušek, T. & Fan, S. Homotopy characterization of non-Hermitian Hamiltonians. *Phys. Rev. B* **101**, 205417 (2020).
32. Li, Z. & Mong, R. S. K. Homotopical characterization of non-Hermitian band structures. *Phys. Rev. B* **103**, 155129 (2021).
33. Hu, H. & Zhao, E. Knots and non-Hermitian Bloch bands. *Phys. Rev. Lett.* **126**, 010401 (2021).
34. Yang, Z., Schnyder, A., Hu, J. & Chiu, C.-K. Fermion doubling theorems in two-dimensional non-Hermitian systems for fermi points and exceptional points. *Phys. Rev. Lett.* **126**, 086401 (2021).
35. Tang, W., Ding, K. & Ma, G. Direct Measurement of topological properties of an exceptional parabola. *Phys. Rev. Lett.* **127**, 034301 (2021).
36. Wang, K., Dutt, A., Wojcik, C. C. & Fan, S. Topological complex-energy braiding of non-Hermitian bands. *Nature* **598**, 59–64 (2021).
37. Hu, H., Sun, S. & Chen, S. Knot topology of exceptional point and non-hermitian no-go theorem. *Phys. Rev. Res.* **4**, L022064 (2022).
38. Wojcik, C. C., Wang, K., Dutt, A., Zhong, J. & Fan, S. Eigenvalue topology of non-hermitian band structures in two and three dimensions. *Phys. Rev. B* **106**, L161401 (2022).
39. Xu, Y., Wang, S.-T. & Duan, L.-M. Weyl exceptional rings in a three-dimensional dissipative cold atomic gas. *Phys. Rev. Lett.* **118**, 045701 (2017).
40. Cerjan, A. et al. Experimental realization of a Weyl exceptional ring. *Nat. Photon.* **13**, 623–628 (2019).
41. Wang, H., Ruan, J. & Zhang, H. Non-Hermitian nodal-line semimetals with an anomalous bulk-boundary correspondence. *Phys. Rev. B* **99**, 075130 (2019).
42. Xiao, Y.-X., Ding, K., Zhang, R.-Y., Hang, Z. H. & Chan, C. T. Exceptional points make an astroid in non-Hermitian Lieb lattice: evolution and topological protection. *Phys. Rev. B* **102**, 245144 (2020).
43. Carlström, J., Stålhammar, M., Budich, J. C. & Bergholtz, E. J. Knotted non-Hermitian metals. *Phys. Rev. B* **99**, 161115 (2019).
44. Zhang, X. et al. Tidal surface states as fingerprints of non-Hermitian nodal knot metals. *Commun. Phys.* **4**, 1–10 (2021).
45. Carlström, J. & Bergholtz, E. J. Exceptional links and twisted Fermi ribbons in non-Hermitian systems. *Phys. Rev. A* **98**, 042114 (2018).
46. Yang, Z. & Hu, J. Non-Hermitian Hopf-link exceptional line semimetals. *Phys. Rev. B* **99**, 081102 (2019).
47. Zhang, Z., Yang, Z. & Hu, J. Bulk-boundary correspondence in non-Hermitian Hopf-link exceptional line semimetals. *Phys. Rev. B* **102**, 045412 (2020).
48. He, P., Fu, J.-H., Zhang, D.-W. & Zhu, S.-L. Double exceptional links in a three-dimensional dissipative cold atomic gas. *Phys. Rev. A* **102**, 023308 (2020).
49. Wang, K., Xiao, L., Budich, J. C., Yi, W. & Xue, P. Simulating exceptional non-Hermitian metals with single-photon interferometry. *Phys. Rev. Lett.* **127**, 026404 (2021).
50. Yan, Z. et al. Nodal-link semimetals. *Phys. Rev. B* **96**, 041103 (2017).
51. Chang, P.-Y. & Yee, C.-H. Weyl-link semimetals. *Phys. Rev. B* **96**, 081114 (2017).
52. Sun, X.-Q., Lian, B. & Zhang, S.-C. Double helix Nodal line superconductor. *Phys. Rev. Lett.* **119**, 147001 (2017).
53. Bi, R., Yan, Z., Lu, L. & Wang, Z. Nodal-knot semimetals. *Phys. Rev. B* **96**, 201305 (2017).
54. Bzdušek, T., Wu, Q., Rüegg, A., Sigrist, M. & Soluyanov, A. A. Nodal-chain metals. *Nature* **538**, 75–78 (2016).
55. Yu, R., Wu, Q., Fang, Z. & Weng, H. From nodal chain semimetal to Weyl semimetal in HfC. *Phys. Rev. Lett.* **119**, 036401 (2017).
56. Chang, G. et al. Topological Hopf and chain link semimetal states and their application to Co₂MnGa. *Phys. Rev. Lett.* **119**, 156401 (2017).
57. Gong, C., Xie, Y., Chen, Y., Kim, H.-S. & Vanderbilt, D. Symmorphic intersecting nodal rings in semiconducting layers. *Phys. Rev. Lett.* **120**, 106403 (2018).
58. Yan, Q. et al. Experimental discovery of nodal chains. *Nat. Phys.* **14**, 461–464 (2018).
59. Xiong, Z., Zhang, R.-Y., Yu, R., Chan, C. T. & Chen, Y. Hidden-symmetry-enforced nexus points of nodal lines in layer-stacked dielectric photonic crystals. *Light: Sci. Appl.* **9**, 176 (2020).
60. Cerjan, A., Xiao, M., Yuan, L. & Fan, S. Effects of non-Hermitian perturbations on Weyl Hamiltonians with arbitrary topological charges. *Phys. Rev. B* **97**, 075128 (2018).
61. Tang, W. et al. Exceptional nexus with a hybrid topological invariant. *Science* **370**, 1077–1080 (2020).
62. Yan, Q. et al. Unconventional Weyl exceptional contours in non-Hermitian photonic continua. *Photon. Res.* **9**, 2435–2442 (2021).
63. Wu, Q., Soluyanov, A. A. & Bzdušek, T. Non-Abelian band topology in noninteracting metals. *Science* **365**, 1273–1277 (2019).
64. Tiwari, A. & Bzdušek, T. Non-Abelian topology of nodal-line rings in PT symmetric systems. *Phys. Rev. B* **101**, 195130 (2020).
65. Bouhon, A. et al. Non-Abelian reciprocal braiding of Weyl points and its manifestation in ZrTe. *Nat. Phys.* **16**, 1137–1143 (2020).
66. Yang, E. et al. Observation of non-Abelian nodal links in photonics. *Phys. Rev. Lett.* **125**, 033901 (2020).
67. Guo, Q. et al. Experimental observation of non-Abelian topological charges and edge states. *Nature* **594**, 195–200 (2021).
68. Wang, D. et al. Intrinsic in-plane nodal chain and generalized quaternion charge protected nodal link in photonics. *Light: Sci. Appl.* **10**, 83 (2021).
69. Yang, Z., Chiu, C.-K., Fang, C. & Hu, J. Jones polynomial and Knot transitions in Hermitian and non-Hermitian topological semimetals. *Phys. Rev. Lett.* **124**, 186402 (2020).
70. Gopalan, V. & Litvin, D. B. Rotation-reversal symmetries in crystals and handed structures. *Nat. Mater.* **10**, 376–381 (2011).
71. Padmanabhan, H., Munro, J. M., Dabo, I. & Gopalan, V. Antisymmetry: Fundamentals and applications. *Annu. Rev. Mater. Res.* **50**, 255–281 (2020).
72. VanLeeuwen, B. K., Gopalan, V. & Litvin, D. B. Double antisymmetry and the rotation-reversal space groups. *Acta Cryst.* **70**, 24–38 (2014).
73. Liang, S.-D. & Huang, G.-Y. Topological invariance and global Berry phase in non-Hermitian systems. *Phys. Rev. A* **87**, 012118 (2013).
74. Frankel, T. *The Geometry of Physics: An Introduction* (Cambridge University Press, 2011).
75. Knöppel, F. *Riemann Surfaces: Complex Analysis from a Differential Geometric Viewpoint* (Lecture Notes, 2020).
76. Mock, A. Characterization of parity-time symmetry in photonic lattices using Heesh-Shubnikov group theory. *Opt. Express* **24**, 22693–22707 (2016).
77. Mock, A. Comprehensive understanding of parity-time transitions in pt-symmetric photonic crystals with an antiunitary group theory. *Phys. Rev. A* **95**, 043803 (2017).
78. Shiozaki, K. & Ono, S. Symmetry indicator in non-Hermitian systems. *Phys. Rev. B* **104**, 035424 (2021).
79. Mostafazadeh, A. Pseudo-Hermiticity versus PT symmetry: the necessary condition for the reality of the spectrum of a non-Hermitian Hamiltonian. *J. Math. Phys.* **43**, 205–214 (2002).
80. Mostafazadeh, A. Pseudo-hermitian representation of quantum mechanics. *Int. J. Geom. Methods Mod. Phys.* **7**, 1191–1306 (2010).
81. Bender, C. M. & Boettcher, S. Real spectra in non-hermitian hamiltonians having PT symmetry. *Phys. Rev. Lett.* **80**, 5243–5246 (1998).
82. Szameit, A., Rechtsman, M. C., Bahat-Treidel, O. & Segev, M. PT-symmetry in honeycomb photonic lattices. *Phys. Rev. A* **84**, 021806(R) (2011).
83. Okugawa, R. & Yokoyama, T. Topological exceptional surfaces in non-Hermitian systems with parity-time and parity-particle-hole symmetries. *Phys. Rev. B* **99**, 041202 (2019).
84. Zhou, H., Lee, J. Y., Liu, S. & Zhen, B. Exceptional surfaces in PT-symmetric non-Hermitian photonic systems. *Optica* **6**, 190–193 (2019).
85. Delplace, P., Yoshida, T. & Hatsugai, Y. Symmetry-protected multifold exceptional points and their topological characterization. *Phys. Rev. Lett.* **127**, 186602 (2021).
86. Mandal, I. & Bergholtz, E. J. Symmetry and higher-order exceptional points. *Phys. Rev. Lett.* **127**, 186601 (2021).
87. Sayyad, S. & Kunst, F. K. Realizing exceptional points of any order in the presence of symmetry. *Phys. Rev. Res.* **4**, 023130 (2022).

88. Hu, J. et al. Non-Hermitian swallowtail catastrophe revealing transitions among diverse topological singularities. *Nat. Phys.* <https://doi.org/10.1038/s41567-023-02048-w> (2023).
89. Lee, J. Y., Ahn, J., Zhou, H. & Vishwanath, A. Topological correspondence between Hermitian and Non-Hermitian systems: anomalous dynamics. *Phys. Rev. Lett.* **123**, 206404 (2019).
90. Fruchart, M., Hanai, R., Littlewood, P. B. & Vitelli, V. Non-reciprocal phase transitions. *Nature* **592**, 363–369 (2021).
91. Peng, J., Zhang, R.-Y., Jia, S., Liu, W. & Wang, S. Topological near fields generated by topological structures. *Sci. Adv.* **8**, eabq0910 (2022).
92. Zhang, R.-Y., Cui, X., Chen, W.-J. & Chan, C. T. Replication data for symmetry-protected topological exceptional chains in non-hermitian crystals. <https://doi.org/10.14711/dataset/KKRJPL> (2023).

Acknowledgements

We thank Profs. Guancong Ma, Biao Yang, Kun Ding, and Shubo Wang for the fruitful discussions. This work is supported by the Research Grants Council of Hong Kong (Grant No. 16303119 and 16307420) and by the Croucher Foundation (Grant No. CAS20SC01). Wen-Jie Chen acknowledges the supports from National Natural Science Foundation of China (Grant No. 11874435), Guangzhou Science, Technology and Innovation Commission (Grant No. 201904010223).

Author contributions

R.-Y.Z. and X.C. developed the theory. X.C. performed the numerical simulations. X.C., R.-Y.Z. and W.-J.C. designed the photonic crystals. R.-Y.Z. and X.C. wrote the manuscript. C.T.C. and Z.-Q.Z. supervised the project. All authors contributed to the discussions and the polishing of the manuscript.

Competing interests

The authors declare no competing interests.

Additional information

Supplementary information The online version contains supplementary material available at <https://doi.org/10.1038/s42005-023-01291-0>.

Correspondence and requests for materials should be addressed to Ruo-Yang Zhang or C. T. Chan.

Peer review information *Communications Physics* thanks the anonymous reviewers for their contribution to the peer review of this work. A peer review file is available.

Reprints and permission information is available at <http://www.nature.com/reprints>

Publisher's note Springer Nature remains neutral with regard to jurisdictional claims in published maps and institutional affiliations.



Open Access This article is licensed under a Creative Commons Attribution 4.0 International License, which permits use, sharing, adaptation, distribution and reproduction in any medium or format, as long as you give appropriate credit to the original author(s) and the source, provide a link to the Creative Commons license, and indicate if changes were made. The images or other third party material in this article are included in the article's Creative Commons license, unless indicated otherwise in a credit line to the material. If material is not included in the article's Creative Commons license and your intended use is not permitted by statutory regulation or exceeds the permitted use, you will need to obtain permission directly from the copyright holder. To view a copy of this license, visit <http://creativecommons.org/licenses/by/4.0/>.

© The Author(s) 2023